Ituarte, Iñigo Flores; Nilsén, Frans; Nadimpalli, Venkata Karthik; Salmi, Mika; Lehtonen, Joonas; Hannula, Simo Pekka

# Towards the additive manufacturing of Ni-Mn-Ga complex devices with magnetic field induced strain

*Published in:*
Additive Manufacturing

*DOI:*
10.1016/j.addma.2021.102485

Published: 01/01/2022

*Document Version*
Publisher's PDF, also known as Version of record

Additive Manufacturing 49 (2022) 102485

Contents lists available at ScienceDirect

Additive Manufacturing

journal homepage: www.elsevier.com/locate/addma

Research paper

# Towards the additive manufacturing of Ni-Mn-Ga complex devices with magnetic field induced strain

Iñigo Flores Ituarte [a,d,*], Frans Nilsén [b,c], Venkata Karthik Nadimpalli [d], Mika Salmi [e], Joonas Lehtonen [f], Simo-Pekka Hannula [f]

[a] Tampere University, Faculty of Engineering and Natural Sciences, Korkeakoulunkatu 6, 33014 Tampere, Finland
[b] Mechanical Engineering and Metals Industry Standardization in Finland (METSTA), Eteläranta 10, PL 10, 00131 Helsinki, Finland
[c] Institute of Physics, Czech Academy of Sciences, Na Slovance 1999/2, 182 21 Prague 8, Czech Republic
[d] Technical University of Denmark, Department of Mechanical Engineering, 2800 Kgs. Lyngby, Denmark
[e] Aalto University, Department of Mechanical Engineering, Otakaari 4, 02150 Espoo, Finland
[f] Aalto University, Department of Chemistry and Materials Science, Kemistintie 1, 02150 Espoo, Finland

ARTICLE INFO

*Keywords:*
Additive manufacturing
Smart materials
Magnetic shape-memory alloys
4D printing
MFIS

ABSTRACT

Laser powder bed fusion (L-PBF) is used to produce foam-like Ni-Mn-Ga with tailored microscale and mesoscale features. Ni50-Mn28.2-Ga21.8 (at%) powder was gas atomised and processed in an L-PBF system with a range of energy density from 26.24 and 44.90 J/mm$^3$. We characterised microscale and mesoscale properties, such as the chemical composition, crystal structure, magnetisation measurements, density, and porosity measurements as a function of process parameters, in a systematic design of experiment. Preliminary research on macroscale properties included tensile testing and magnetic field induced strain (MFIS) measurements. Results show how controlling process parameters allows tailoring the Ni-Mn-Ga polycrystalline microstructure. Hence, obtaining twinned martensitic structures with a predominant orientation going across the visible grain boundaries. All the processed samples showed a 56 Am$^2$/kg magnetisation level, close to Ni-Mn-Ga 10 M single crystals. Mesoscale results show a distinctive porosity pattern that is tailored by the process parameters and the laser scanning strategy. In contrast, macroscale mechanical tensile test results show a brittle fracture of Ni-Mn-Ga due to the high porosity with yield stress 2–3 times higher than shown in single crystals. In sum, we built geometrically complex demonstrators with (i) microscale twinned martensitic structures with a predominant orientation going across the visible grain boundaries and (ii) mesoscale tailored periodic porosity patterns created by modifying power, scanning speed, and scanning strategy systematically. L-PBF demonstrates great potential to produce foam-like polycrystalline Ni-Mn-Ga, reducing grain boundary constraints and thus the magnetic force needed for MFIS.

## 1. Introduction

Ni-Mn-Ga ferromagnetic alloy systems are the most common Magnetic Shape Memory (MSM) materials. The shape change occurs via the twin boundary motion in the twinned martensitic Heusler structure [1–3]. Twinning in functional MSM single-crystal material is intertwined with a significant mechanical strain, which can be induced by magnetic or thermal energy [4–6]. The study of Ni-Mn-Ga MSM alloys started in 1996 with the discovery of its properties by Ullakko et al. [7]. However, during more than two decades of research, only a limited amount of industrial applications have emerged [8,9] and currently, there is only one commercial manufacturer on the market that can supply functional Ni-Mn-Ga single crystals [10].

The lack of commercial applications is related to the difficulties in industrial-scale manufacturing of Ni-Mn-Ga single crystals. The challenges include (i) the low vapour pressure of manganese [11], which leads to its evaporation during manufacturing and difficulties in controlling the composition and structure of the crystal, (ii) the high cost of the alloying elements, and (iii) the demand of many labour-intensive manufacturing steps and heat treatments [12].

Since 2016, the research on Additive Manufacturing (AM) of shape memory alloys (SMA) and particularly magnetic Ni-Mn-Ga alloys has

* Corresponding author at: Tampere University, Faculty of Engineering and Natural Sciences, Korkeakoulunkatu 6, 33014 Tampere, Finland.
*E-mail address:* inigo.floresituarte@tuni.fi (I.F. Ituarte).

https://doi.org/10.1016/j.addma.2021.102485
Received 17 August 2021; Received in revised form 21 October 2021; Accepted 9 November 2021
Available online 18 November 2021

rapidly increased [13–21]. The technology shows potential for materials and geometries challenging to manufacture using conventional methods [22]. It enables a wide range of processing techniques and micro and mesoscale tailoring capabilities [23], which are well suited for smart materials (i.e., materials that can transform their geometry under the influence of external stimuli) [24]. The body of research shows that SMA materials have been processed by (i) Directed Energy Deposition [13, 17], (ii) Binder Jetting [14,15], (iii) Material Extrusion [16], and (iv) Laser Powder Bed Fusion (L-PBF) [18–21].

The real advantage of AM is its *"ability to maximise product performance through the synthesis of shapes, sizes, hierarchical structures, and material compositions, subject to the constraints and capabilities of the particular AM process"* [25]. L-PBF can create complexity enhanced smart materials for microelectromechanical systems, such as highly customised low-frequency vibration-damping elements, piezoelectric materials for reduced size devices such as micro-actuators with complex external and internal geometries, microfluidics for the precise dosing of liquids, as well as MEMS or other kinds of sensors.

In the specific case of L-PBF, the process is constrained by the fast cooling rates and spatially varying temperature gradients during the layer by layer build process that ultimately creates complex microstructures [26] and residual stress states [27]. For instance, in 316L stainless steel, L-PBF processed metals frequently exhibit high dislocation densities, segregation of elements, fine solidification structures, and elongated columnar grains in the build direction [23]. On the other hand, process parameters in L-PBF can be used to influence the directional solidification of the materials (e.g., by a combination of effective power, scanning speed, scanning patterns, or laser beam shaping strategies) [28,29]. One of the advantages of L-PBF, when combined with heat treatment procedures, is the possibility to tailor microscale features (1–100 μm) and mesoscale features (100 μm to 1 mm) during the build process [26]. Multiple research examples show how tailoring of micro and mesoscale features, such as microstructure texture and porosity, is achievable by modifying L-PBF process parameters [31,2230].

Understanding process-structure-property relationships between machine and process parameters, material chemical composition and morphology, and ultimately post-processing strategies, such as annealing, could be used to control the micro and mesoscale features [28,32]. Yet, tailoring at micro and mesoscale could be used to produce foam-like geometrically complex Ni-Mn-Ga devices that could effectively show macroscale magnetic field induced strain (MFIS) [33]. L-PBF is thus well poised to usher the next generation of functionally graded smart materials through innovations in materials and process development [34].

Nilsén et al. [20] have shown that after the initial L-PBF process, the as-sintered Ni-Mn-Ga samples exhibit paramagnetic behaviour. For the same reason, the Ni-Mn-Ga samples require homogenisation and ordering heat treatment to recover the original structure and magnetic properties. In summary, this previous research pointed towards the need for testing a more extensive range of volumetric energy density.

The initial hypothesis is that a delicate trade-off optimisation is required to produce foam like Ni-Mn-Ga structures by L-PBF, with fewer grain boundary constraints, which potentially leads to a large MFIS effect at the macroscale [14,18,20]. This research presents how tailoring microscale and mesoscale features as a function of L-PBF process parameters is possible. Furthermore, the viability of L-PBF to manufacture large complex geometries made of Ni-Mn-Ga with overhang features is studied and demonstrated. Besides, we research several areas of interest to design and manufacture a geometrically complex demonstrator device manufactured by L-PBF in 10 M Ni-Mn-Ga powder.

In summary: (i) we present an L-PBF process parameter study focused on understanding the densification process and porosity formation during the build process with a range of energy density from 26.24 and 44.90 J/mm$^3$. (ii) We research the changes in material composition during the L-PBF process and the process chain, including its heat-treatment process. The original material composition can change due to high volumetric energy density causing the evaporation of alloying elements. With Ni-Mn-Ga, manganese evaporation is common during manufacturing or annealing due to its relatively high vapour pressure compared with nickel and gallium [20]. (iii) The microscale and mesoscale properties such as the texture, microstructure, and porosity distribution as a function of L-PBF process parameters are determined using XRD, SEM and X-ray CT for characterisation. Recent research by Laitinen et al. [35] shows that a systematic study is required to manufacture foam-like structures with enhanced crystallographic texture. (iv) The magnetisation and phase transformation temperatures for laser PBF processed Ni-Mn-Ga samples were obtained using a vibrating sample magnetometer (VSM) and low-field ac susceptibility measurement device. These parameters are critical to achieving room temperature MFIS. (v) Finally, we present preliminary results on the macro mechanical behaviour of the manufactured samples and results for MFIS training of the samples, while a set of future research directions is outlined.

## 2. Materials and methods

### 2.1. Ni-Mn-Ga powder

Gas atomised powder as Ni50-Mn28.2-Ga21.8 (at%) is used to form the original composition. The composition measurement was performed using an FEG-SEM from Tescan Mira 3 FEG-SEM with an attached Thermo Fisher Scientific UltraDy EDX detector. The measurement procedure utilised a sample with a known composition as a reference. The powder was atomised with a Hermiga lab-scale gas atomiser. The atomising gas was argon. Atomisation parameters were: Processing temperature of 1310 °C and atomising pressure of 50 bar. The powder density was measured using a gas pycnometer. It resulted in a density of 7.91 g/cm$^3$. Fig. 1(b) shows that the particle size has a normal distribution, and the measurement results show a D10 of 15.41 μm, D50 of 42.78 μm, and a D90 of 92.05 μm.

The atomised powder was mechanically sieved to obtain a theoretical particle size distribution from 25 μm to 45 μm. The morphology of the sieved powder was inspected with the Tescan Mira SEM. Further, the powder's particle size distribution was measured using Malvern Mastersizer 3000. The powder was heat-treated at the salt bath at 760 °C for 24 h [12]. The resulting powder had excellent flow properties, which was proved qualitatively by spreading within the L-PBF machine itself. Fig. 1(a) shows how the powder morphology (i.e., particle shape and size) consisted mainly of spherical particles with minor irregularly shaped satellites and spatters.

### 2.2. Laser powder bed fusion process

The Ni-Mn-Ga was processed in a Mlab Cusing (Concept Laser, Germany) L-PBF system with a fixed layer thickness of 0.025 mm and a building envelope of 90 × 90 × 80 mm$^3$. Fig. 2 shows the representation of the L-PBF system and the island scanning strategy implemented in this study. Fig. 2(a) shows the schematic 3D view of a laser PBF system along with the main components. The PBF system was equipped with a 100 W Ytterbium Fiber Laser (Model YLM-100-AC). The laser has a Gaussian beam with an average wavelength of 1070.15 nm and standard deviation of 0.69 nm, laser beam focus diameter of 54 μm, and a maximum scanning speed of 7000 mm/s. Argon gas was used as a protective atmosphere while maintaining the oxygen levels $< 0.1\%$.

The island scan strategy divides the XY section of the layer into squares of 5 × 5 mm, forming the pattern shown in Fig. 2(b). Each of these islands is then fused in a randomised sequence. The scan vectors have a predefined hatch distance (A1*W) is used within each of the islands. The scanning vectors in the adjacent islands are perpendicular to each other.

Fig. 2(c) shows the detailed representation of a single island with its corresponding overlapping regions with a track width of 140 μm (W) and a laser scan track overlap factor A1 = 0.7 that represents a hatch

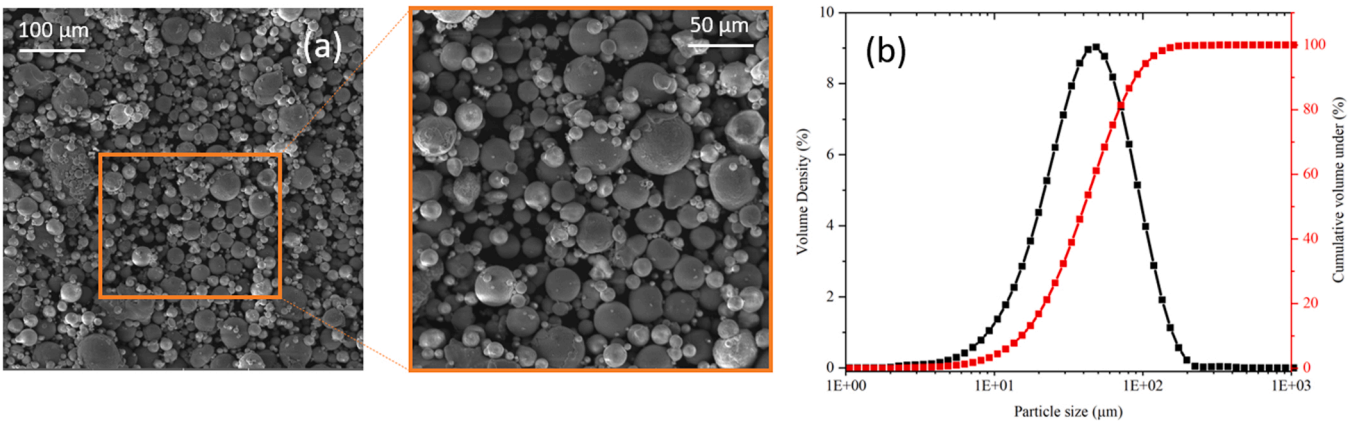


**Fig. 1.** (a) Scanning electron microscope (SEM) images of the sieved powder and (b) Particle size distribution (PSD) of the sieved Ni-Mn-Ga powder.

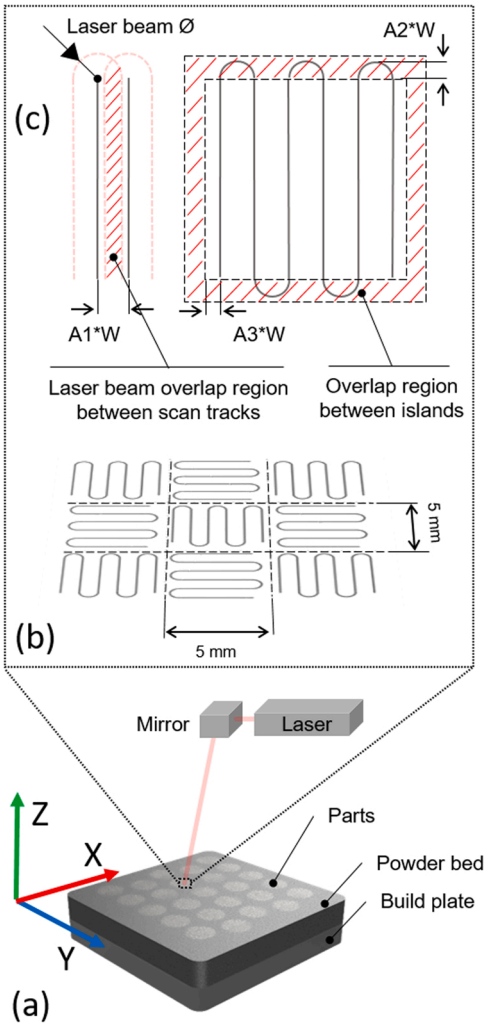


**Fig. 2.** Representation of the laser PBF process, (a) Schematic 3D view of a laser PBF system along with the components, (b) the island scanning pattern, and (c) representation of a single island with its corresponding overlapping regions.

distance of 98 µm (A1*W). The overlap factors A2 and A3 ensure that the islands are connected with an A2 = A3 = 0.15. For every layer, the island pattern is shifted by 1 mm in both the X and Y direction, and rotated by 90° with reference to the XY plane.

### 2.3. Design of experiment for process parameters screening

The relationship between L-PBF process parameters is typically modelled by a thermodynamic parameter defined as volumetric energy density (ED), which is measured in energy per volume of material (i.e., J/mm$^3$) and refers to the relative applied laser. Although ED does not fully explain the complex physical phenomena connected with the densification or changes in chemical composition during laser-based PBF, it is often used as a reference variable to optimise process parameters and is calculated using Eq. (1):

$$ED = \frac{P_{eff}}{v * h * d} \quad (1)$$

Where ($P_{eff}$) refers to the effective laser power, ($v$) is the laser scan speed, ($h$) is the hatch distance or the laser scan spacing, and ($d$) is the layer thickness. A full factorial Design-of-Experiment (DOE) is performed to model the effect of process parameters over the responses. Table 1 shows the included process parameters and levels.

In previous experiments with Ni-Mn-Ga powder and the same L-PBF setup, we tested an ED range from 17.49 and 32.65 J/mm$^3$ [20]. This research focussed on a new ED region of interest, which varied from 26.24 and 44.90 J/mm$^3$. The reason is to obtain an operational model to predict the porosity level of the material as a function of the process parameters with a more extensive energy range.

The statistical modelling is limited to explaining the variation in (i) density and (ii) material composition. We calculate the variation in material composition results from Mn evaporation as the percentage of evaporation between the resulted at% of Mn after L-PBF of heat-treated (HT) samples versus the original at% of Mn. As a result, the compositional variation of Mn remains equal when the obtained percentage value is zero. The result of density measurement is used as the second response. The rationale to measure the change in material composition and densification process is based on the existing trade-off due to the evaporation of alloying elements at higher energy density.

Three types of samples were manufactured in a single batch of cuboids, tensile rods, and SMA demonstrators to perform the experiments. Fig. 3(e) shows the manufactured batch of tensile rods, cuboids, and SMA device demonstrators manufactured with different process parameters in the same build. All Ni-Mn-Ga samples, cuboids, demonstrators, and tensile rods are manufactured simultaneously and follow the same DOE procedure. The numbering in the picture and samples

**Table 1**
DOE for process parameter screening.

| Process parameter | Abbreviation | Levels | | |
|---|---|---|---|---|
| Power | P (W) | 45 | 50 | 55 |
| Scanning Speed | v (mm/sec) | 500 | 600 | 700 |

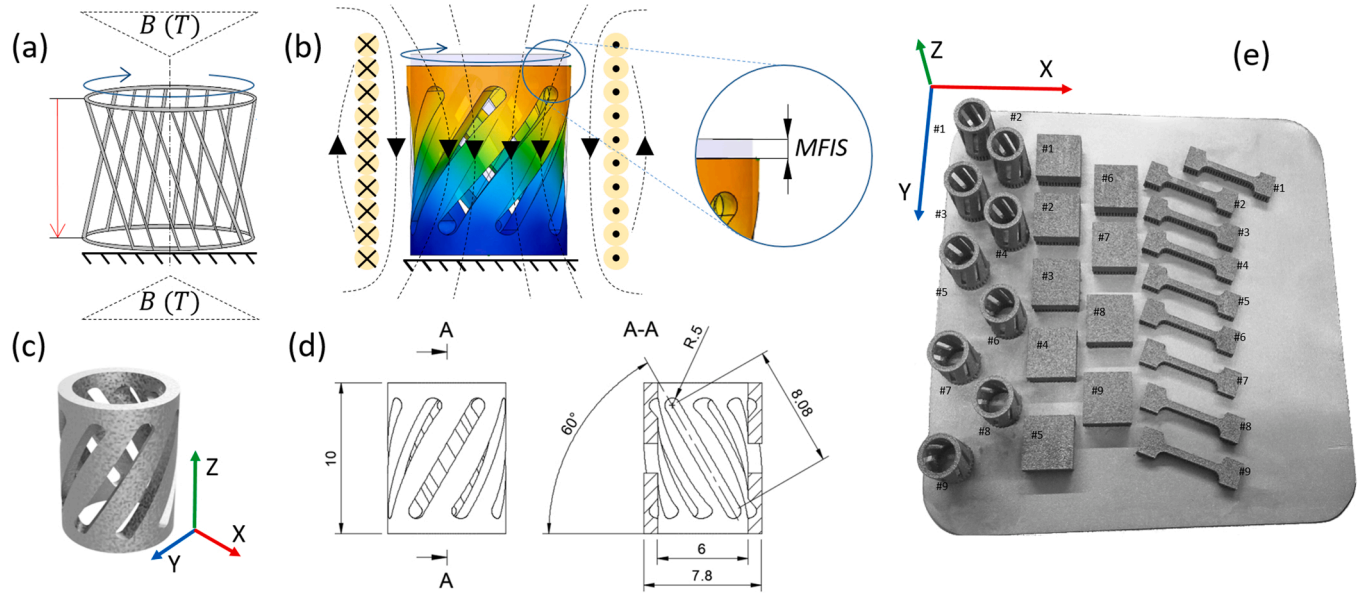


**Fig. 3.** (a) Conceptual drawing of the SMA demonstrator and its working principle, (b) simulated demonstration of the MFIS effect, (c) CAD of the SMA demonstrator, (d) 2D drawings and dimensions in mm of the SMA device, and (e) an exemplary batch of tensile rods, cuboids, and SMA device demonstrator manufactured with different process parameters in the same build.

corresponds to the sample number described in Table 2.

Additionally, Fig. 3(a) and (b) show the working principle of the manufactured SMA device with the simulated MFIS effect. Fig. 3(c) and (d) show the CAD and overall dimensions of the SMA demonstrator, showcasing its macroscale geometrical complexity, including overhanging features that could benefit the desired MFIS effect. The coordinate system is displayed in Fig. 3(c) and (e), where the Z-axis corresponds to the build direction during the L-PBF process. The X-axis corresponds to the recoating direction, and the XY plane is the perpendicular plane to the build direction, where the layers of Ni-Mn-Ga are deposited.

Each of the samples was manufactured for each parameter set, as described in Table 2. A batch of SMA demonstrators was fabricated to demonstrate the possibility of manufacturing complex SMA devices using Ni-Mn-Ga powder. The cuboid samples were cut into several parts with a wire Electric Discharge Machining (EDM) to perform the as-built and heat-treated state measurements. The original size of the cuboids had dimensions of $1 \times 1 \times 0.5$ cm$^3$. Additionally, miniature tensile rods were fabricated to evaluate macro mechanical response.

An ANOVA test with a confidence level of 95% ($\alpha = 0.05$) was included. The data was used to build multivariable polynomial regression equations to explain the variation of Density (%)and Mn (%) evaporation as a function of the principal process parameters (power, velocity). The ANOVA test included first-order, second-order, and interaction terms. The experimental data was fitted to a polynomial response surface model (RSM) defined below in Eq. (2).

**Table 2**
Powder bed fusion parameters and volumetric energy density per sample.

| Sample # | Power (W) | Scan speed (mm/sec) | ED (J/mm$^3$) |
|---|---|---|---|
| SMA #1 | 45 | 500 | 36.73 |
| SMA #2 | 45 | 600 | 30.61 |
| SMA #3 | 45 | 700 | 26.24 |
| SMA #4 | 50 | 500 | 40.82 |
| SMA #5 | 50 | 600 | 34.01 |
| SMA #6 | 50 | 700 | 29.15 |
| SMA #7 | 55 | 500 | 44.89 |
| SMA #8 | 55 | 600 | 37.41 |
| SMA #9 | 55 | 700 | 32.07 |

$$y = \beta_o + \sum_{i=1}^{k} \beta_i x_i + \sum_{i=1}^{k} \beta_{ii} x_i^2 + \sum_i \sum_j \beta_{ij} x_i x_j + \varepsilon \quad (2)$$

Where $\varepsilon$ is the unobserved random error, $\beta$ refers to the coefficients of the regression model for each term calculated by the least square method (i.e., intercept $\beta_0$, first-order $\beta_i$, second-order $\beta_{ii}$, and the interaction term $\beta_{ij}$), $x_i$ represent the independent variables P and v. The interaction terms between independent variables are represented by $x_i$ $x_j$, and y corresponds to the dependent Density (%) and Mn (%) evaporation. To remove non-significant terms from the RSM, we used a stepwise regression with a forward stopping rule of a P-value $< 0.5$.

### 2.4. Measurements and characterisation work

#### 2.4.1. Heat treatment process

Half of the cuboids were sealed in evacuated crystal ampoules with a high vacuum with the tensile samples. The samples were then annealed in a Nabertherm Muffle furnace (model L5/12/C). The homogenisation annealing took 95 h at 1000 °C and was followed by ordering for 24 h at 800 °C. The remaining cuboids were left in the as-sintered stage for comparison.

In addition to chemical homogenisation and ordering, the objective was to increase the grain size of the printed samples. We used a heating and cooling rate of 100 °C/h, and the samples were left into the furnace to cool until 20 °C. The annealing process was the same as that used by Nilsén et al. [20]. Recent research by Laitinen et al. [35] shows evidence that a slight variation in homogenisation time and the temperature does not affect magnetic properties as long as the temperature and HT procedure is maintained, similar to what was previously presented Nilsén et al. [12].

#### 2.4.2. Microscale: chemical composition, crystal structure, and magnetisation measurements

A Tescan Mira 3 FEG-SEM was used with a Thermo Fisher Scientific UltraDry EDX detector, with a Ni-Mn-Ga sample of known composition as a reference to study the chemical composition by measuring several points and line scans. The standardised EDX analysis was done with NSS microanalysis System - Pathfinder, which has an accelerating voltage at 30 kV. The average chemical composition was accurately quantified

through several measurements.

Concerning microscale characterisation, the PANalytical X'Pert Pro XRD was used to study the crystal structures. Additionally, multiple Scanning Electron Microscope (SEM) images were taken to analyse the crystal structure, grain morphology, and the formation of martensitic twins. The phase transformation temperatures were determined by measuring the change in magnetisation as the temperature was cycled from 0° to 120°C three times using a custom-built setup for low-field AC susceptibility measurements. Furthermore, the magnetic properties characterisation was performed using a NIST nickel disk as a reference sample using laboratory-built vibrating sample magnetometer (VSM) equipment. All measurements were done at room temperature of approximately 22 °C. Please refer to Nilsén et al. [20] for more details on the assessment of the average chemical composition, crystal structure, and magnetisation measurements.

### 2.4.3. Mesoscale: density and porosity measurements

The densities of all the samples were first measured by the Archimedes method. To study the mesoscale structure in more detail, some of the samples were also X-ray CT scanned. The X-ray CT scanning measurements were used to reveal the distribution and size of porosity across the samples and study the porosity morphology. We wanted to investigate the morphology of porosity as a function of process parameters P and v to classify the porosity into three types. The first is layered porosity, the second is the interconnected porosity across layers, and the third is the gas porosity induced by keyhole formation or insufficient melting.

Three samples were prepared with varying ED levels (i.e., low-SMA #3 26.24 J/mm$^3$, mid-SMA #5 34.01 J/mm$^3$, and high-SMA #7 44.09 J/mm$^3$), which were cut from the original cuboids. A Nikon X225 μfocus X-ray CT system was used on the ~3 × 6 × 3 mm$^3$ specimens with an energy of 200 keV and a power of 15 W to achieve a voxel size of 11.54 μm. Standard calibration procedures for background noise reduction were followed, and a slow scan with ring artefact removal was performed. X-ray CT figures show their vertical and horizontal axis units in pixels, where 100 pixels correspond to approximately ~ 1.22 mm.

The CT data was reconstructed using the Nikon CTpro3D software, wherein beam hardening compensation was applied. The volume graphics file was analysed in MATLAB through manual thresholding and a 3D connected components analysis. The volume file was first sliced and processed using a median filter. An outer mask of the part was generated with morphological closing using a circular disk element of 30 voxels. A manual threshold range was selected, and the slice data were converted to binary images. A connected components analysis was used to label each independent porosity, as shown in Fig. 4.

There are two distinct kinds of porosity, which are formed during the L-PBF process. The first is interconnected porosity with a strong anisotropy in the build direction; see Fig. 4(a). The second is randomly distributed spherical porosity across the sample; see Fig. 4(b). Fig. 4(e) showcases large interconnected porosity, while other colours represent smaller and more spherical porosity. Each identified porosity can be independently analysed for its volume, surface area, sphericity, etc. Thus, the pores were divided into those with sphericity greater or less than 0.5. The effective volume of the bounding box (generated from a morphological closing outer mask), together with the total sum of the volume of all pores, gives the Density of the component.

### 2.4.4. Macroscale: preliminary mechanical and MFIS characterisation trials

The mechanical characterisation was performed using an in-house design universal thermomechanical testing rig for macroscale observations. The rig consists of a loading frame, sample environment chamber, electrically conductive grips with active water cooling, a load-cell with 45 N tension and compression capacity, a linear actuator controlled with magnetic position sensor, and a precision class of ± 10 μm/m. The electrically conductive grips were used in combination with electric resistance measurements in-situ during tensile testing. The testing rig and stress, strain or temperature tests were controlled and recorded via National Instruments cRIO and close-loop Labview control systems. In our case, the testing temperature was 20 °C and a crosshead displacement rate of 0.002 mm/sec. Additionally, deformation was also measured optically on the gauge section using a digital image correlation (DIC) built to use scientific cameras and adequate lenses to nearly simulate optical microscope observations.

To increase the MFIS effect, initially, magneto-mechanical training was attempted with two samples using an electromagnet and mechanical compression [36]. During the training regime, samples were heated above austenite temperature and then cooled down in a 1 T magnetic

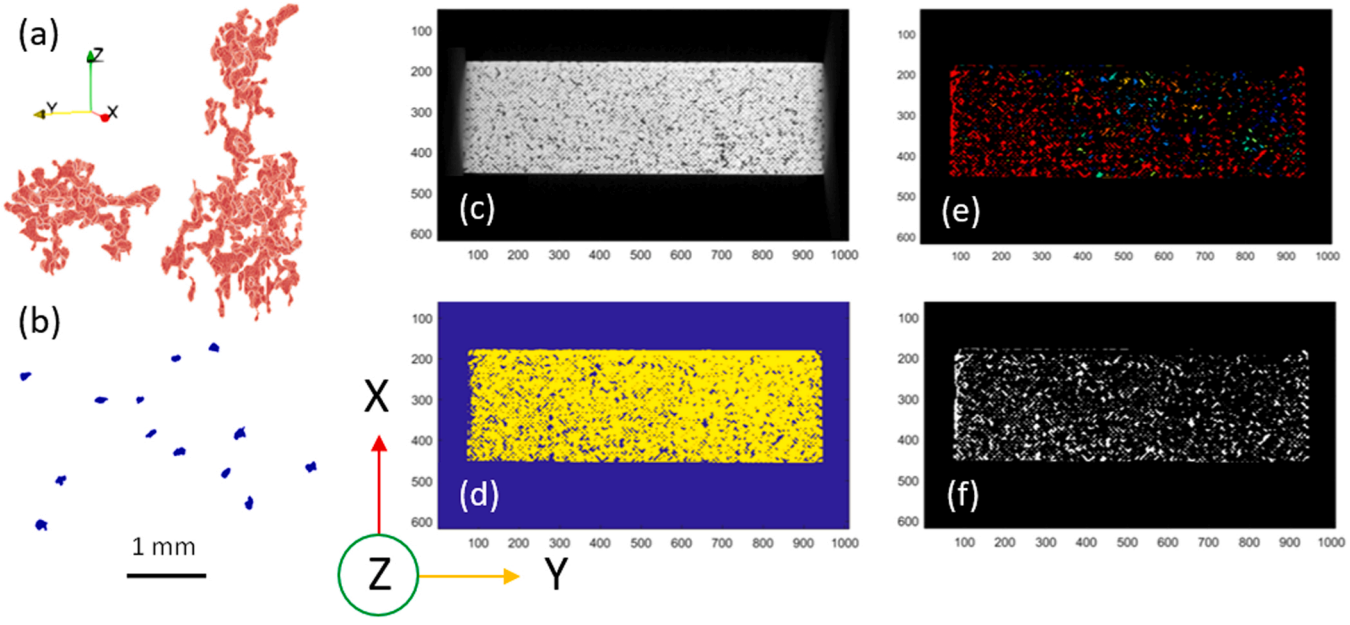


**Fig. 4.** X-ray CT scanning process. (a) Interconnected porosity with anisotropy in the Z direction, (b) spherical porosity voids across the sample, (c) reconstructed CT data of ~ 3 × 6 × 3 mm$^3$ samples, (d) thresholding and the slice data converted to binary images, (e) connected components analysis to label each independent porosity, and (f) total porosity. From (c) – (f), the XY plane is shown in the figure, with build direction Z ~ 1.5 mm from the support structures.

**Table 3**
Chemical composition after heat treatment measured with EDX, and Archimedes density measurement with the standard error of means, and e/a-ratio per sample.

| | | | | Chemical composition (at%) | | | | |
|---|---|---|---|---|---|---|---|---|
| Sam. # | P (W) | v (mm/sec) | ED (J/mm$^3$) | Ni (at%) | Mn (at%) | Ga (at%) | Archimedes Density (%) | e/a |
| SMA #1 | 45 | 500 | 36.73 | 50.20 ± 0.05 | 27.90 ± 0.05 | 21.89 ± 0.06 | 91.07 ± 0.59 | 7.63 |
| SMA #2 | 45 | 600 | 30.61 | 50.11 ± 0.09 | 28.16 ± 0.06 | 21.73 ± 0.09 | 88.16 ± 0.56 | 7.63 |
| SMA #3 | 45 | 700 | 26.24 | 50.01 ± 0.05 | 28.01 ± 0.05 | 21.97 ± 0.07 | 85.51 ± 0.59 | 7.62 |
| SMA #4 | 50 | 500 | 40.82 | 50.31 ± 0.06 | 27.82 ± 0.06 | 21.86 ± 0.05 | 93.84 ± 0.64 | 7.63 |
| SMA #5 | 50 | 600 | 34.01 | 50.46 ± 0.06 | 27.71 ± 0.07 | 21.82 ± 0.08 | 90.81 ± 0.58 | 7.64 |
| SMA #6 | 50 | 700 | 29.15 | 50.66 ± 0.07 | 27.86 ± 0.05 | 21.48 ± 0.08 | 86.47 ± 0.67 | 7.66 |
| SMA #7 | 55 | 500 | 44.90 | 50.80 ± 0.06 | 27.51 ± 0.05 | 21.69 ± 0.08 | 95.91 ± 0.62 | 7.66 |
| SMA #8 | 55 | 600 | 37.41 | 50.73 ± 0.07 | 27.81 ± 0.05 | 21.46 ± 0.09 | 93.66 ± 0.60 | 7.66 |
| SMA #9 | 55 | 700 | 32.07 | 50.68 ± 0.07 | 27.83 ± 0.04 | 21.48 ± 0.04 | 91.50 ± 0.58 | 7.66 |

field along its x-axis to below 0 °C using a cooling stage. Once the sample had magnetised thusly, the field was removed, and samples were compressed along its y-axis up to a total strain of 0.05%. After this compression, the samples were re-magnetised along the x-axis. However, due to the fragile nature of the samples, several samples were broken or damaged during this magneto-mechanical training cycle, and thus the magneto-mechanical test could not be used reliably for MFIS validation.

Alternatively, additional samples were prepared by cutting 1 × 1 × 0.5 mm rods. Due to the small size of the samples and the available measurement systems, MFIS of the samples was attempted by using an optical measurements setup. A similar method was previously utilised by Nilsén et al. [12]. The samples were required to be electropolished at − 30 °C using a solution of nitric acid and alcohol. The optical MFIS measurements were performed for each sample, and for the measurement, an electromagnet with a rotating heating stage was used. Samples were attached to the rotating stage using double-sided 3 M tape so that the field was along the x-direction of the sample. To be able to record MFIS at the macro scale, a camera was placed so that it could be focused directly on the XY plane. Once the camera was focused, the magnetic field was increased to 1 T, and the sample was rotated so that sample was magnetised along the x-axis followed by the y-axis. The sample was filmed during this rotation, and as the original length of the sample was known, hypothetically, the MFIS could be measured using the ImageJ analysis program.

## 3. Results and discussion

### 3.1. Chemical composition, density, and crystal structure

Table 3 shows the resulting chemical composition, e/a ratio, and Archimedes density after heat treatment of the samples. Similar to the previous research [20], some manganese evaporated during the combined manufacturing step of L-PBF and heat treatment. Typically some manganese evaporation is expected, and the amount is within expected limits. Increasing the ED and the heat treatment led to a higher density than the previous research [20].

Additionally, the Mn loss increases the e/a-ratio [37] of the samples from the original e/a of 7.628 of the base powder. The e/a-ratio of the samples stays within the expected 10 M range of 7.62–7.68 [38] for Ni-Mn-Ga alloys. This slight shift to a higher e/a ratio can even be beneficial for the application, as this can increase the martensitic transformation temperature of the alloys and widen the application temperature range of the alloy. This increase comes at the expense of lowering the Curie temperature and the magnetisation of the alloys.

Overall, the evaporation of Mn does not indicate a large change in

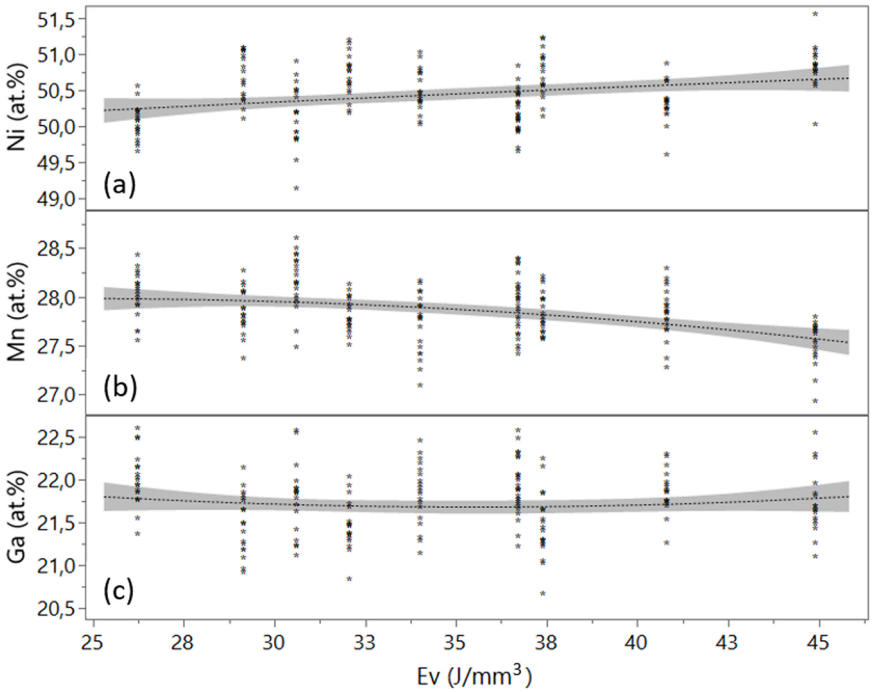


**Fig. 5.** Effect of volumetric energy density on chemical composition obtained by EDX from heat-treated Ni-Mn-Ga cuboid samples. (a) Ni (at%), (b) Mn (at%), and (c) Ga (at%).

**Table 4**
XRD based lattice parameters a, b, and c for all manufactured samples The crystal structure is slightly orthorhombic with space group Fmmm (69) $\alpha = \beta = \gamma = 90°$).

| | SMA #1 | SMA #2 | SMA #3 | SMA #4 | SMA #5 | SMA #6 | SMA# 7 | SMA #8 | SMA #9 |
|---|---|---|---|---|---|---|---|---|---|
| a (Å) | 5.93 | 5.93 | 5.93 | 5.92 | 5.93 | 5.92 | 5.96 | 5.93 | 5.92 |
| b (Å) | 5.97 | 5.95 | 5.95 | 5.95 | 5.96 | 5.95 | 5.93 | 5.97 | 5.95 |
| c (Å) | 5.58 | 5.57 | 5.59 | 5.57 | 5.58 | 5.57 | 5.58 | 5.59 | 5.57 |

the chemical composition regardless of the increase of volumetric energy density (i.e., ED). Fig. 5 illustrates that the low ED samples are compositionally close to the initial powder (i.e., Ni 50 at%, Mn 28.2 at %, and Ga 21,8 at%). On the other hand. when ED increases the trend shows a marked decrease in the fraction of Mn, whereas the fraction of Ni increases and the fraction of Ga remains similar.

The crystal structure of the samples was confirmed using XRD, following the compositional analysis of the samples, and as expected, all the heat-treated samples showed 10 M structure. The crystal structure was calculated from the XRD spectra using Powder Cell for each sample (see Table 4). Even with the slight change in the composition within the samples, the crystal structure is relatively homogenous from sample to sample. Thus, it can be concluded that the heat treatment procedure following the laser PBF step ordered and homogenised the structure adequately.

When the microstructure was studied using the SEM, visible twins could be seen in all the samples (see Fig. 6). In many areas, the twins spanned large regions of the polycrystalline structure and had a similar orientation to nearby grains. The SEM images displayed are taken perpendicular to the XY plane.

Twinned martensitic structures could be observed clearly in all the samples, and the twin formations develop on both sides of the visible grain boundaries. Fig. 6(f) shows a major internal twin variant marked with a dashed line. In sum, the L-PBF processed Ni-Mn-Ga revealed a clear texture and polycrystalline structure, and all samples showed open pore structures. The grain growth is oriented towards the build direction. The SEM images reveal qualitatively how porosity decreases as the ED increases.

### 3.2. Predictive modelling for changes in Mn evaporation (%) and density (%)

Table 5 shows the ANOVA table for Mn evaporation (%) and Density (%) after heat treatment, including the laser power (P) and scanning velocity (v) terms as continuous predictors. P-value is used to quantitatively evaluate the correlation effect of process parameters P and v over the Density (%) and Mn (%) evaporation responses.

Table 6 shows the regression equations that explain the variation in Density (%), and Mn (%) evaporation as a function of process parameters. The polynomial RSM includes first-order terms for P and v, a second-order term for P, and the interaction effect between P * v for both Density (%) and Mn (%) evaporation. In the densification process, the model summary shows a good fit with an increased $R^2 = 0.977$ and a low RMSE of 0.742, which corresponds to a datum of Density that ranges from 0% to 100% (i.e., fully dense part). The ability of the model to predict the response for new observation is also high, with an $R^2$(adj.) $= 0.955$. On the other end, in the Mn (%) evaporation modelling, the fitness decreases to $R^2 = 0.764$ with an RMSE of 0.43. Similarly, the prediction response for new observation decreases to $R^2$(Adj.) $= 0.53$.

Although it appears to be a clear trend between the increased effect of ED and the change of material composition of Ni-Mn-Ga samples after heat treatment, the effects of the applied process parameters on Density (%) and Mn (%) evaporation are significantly different. Fig. 7 shows the RSM model's results on sample density (%) and Mn (%) evaporation after heat treatment per level of P and v process parameters. The color gradient in the legend indicates the change in ED. Additionally, the model displays the density ellipsoid assuming the bivariate normal distribution with a coverage of 90%. The density ellipsoid is used as an indicator of the correlation between Mn (%) evaporation and Density (%), thus capable to visualise where a given percentage of new observations is expected to lie.

Fig. 7(a) shows how increasing ED has a penalty of changing the original Mn content—on the other hand, increasing ED results in higher Density (%). The y-axis corresponds to the Mn (%) evaporation, and the x-axis shows the Density (%) of manufactured samples by displaying both the experimental results and predicted results using equations in Table 6. Pearson correlation (r) shows a negative correlation between (%) Mn evaporations and Density (%) of the samples. Thus, the increase in (%) Density harms (%) Mn evaporation. Similarly, Fig. 7(b) and (c) shows the contour plots of the RSM models for Density (%) and Mn (%) evaporation, respectively. Low P and high v values are responsible for reduced Density (%) and Mn (%) evaporation (i.e., Density $< 86\%$ and Mn evaporation $\geq$ - 0.8% with an ED $= 26.24$ J/mm$^3$). On the contrary, high P and low v values increase the Density (%) at the cost of increased Mn (%) evaporation (i.e., Density $\geq 96\%$ and Mn evaporation $< -2.2\%$ with an ED $= 44.90$ J/mm$^3$).

Increased Density (%) comes at the cost of changing the original chemical composition slightly. This same trade-off is described in previous research [12,18,20]. Increased Density of Ni-Mn-Ga samples at higher ED comes at the cost of changes in chemical composition by decreasing the original Mn content and the corresponding higher concentration of Ni. An alternative approach to maintain Mn (at%) close to the original composition of 28.8 (at%) is to design a Ni-Mn-Ga powder compound by over-alloying the Mn content to counteract the observed loss. The RSM model is capable of explaining the variability on Density (%) with high certainty. However, it cannot provide a good prediction for Mn (%) evaporation, with $R^2 = 0.764$. The use of the RSM model is significantly linked to the ability to predict Density (%), and it can be used to predict porosity reliably in future experiments when experimental methods and materials are the same.

### 3.3. CT results and porosity morphology

For the study of the mesoscale features (i.e., porosity morphology from 100 μm to 1 mm), the X-ray CT scanning was limited to the study of three samples processed at different ED levels (i.e., low ED SMA #3 26.24 J/mm$^3$, mid ED SMA #5 34.01 J/mm$^3$, and high ED SMA #7 44.09 J/mm$^3$). Fig. 8 shows the two types of porosities classified as spherical and large interconnected porosity and the total porosity for the three samples with varying ED.

The spherical pores had a much smaller average volume than the interconnected pores in the three samples analysed. The interconnected porosity has the most volume, and in some cases, a single interconnected pore can span the whole component like in the low-density case. The amount of interconnected porosity drastically increased with decreasing ED. The amount of spherical porosity gradually increased with decreasing ED. Spherical porosity is distributed across the sample and has its centroid near preferred XY locations in each Z slice of the sample, where Z is the build direction. The reason could be due to the scan strategy. The Density calculated from the CT validated the experimentally measured Archimedes density.

The unique behaviour of the interconnected porosity with a build directional anisotropy indicates that the defects created during the L-PBF process were amplified during the heat treatment process. The large interconnected pores indicate that existing porosity acted as preferential sites for manganese to escape, thus forming the interconnected porosity.

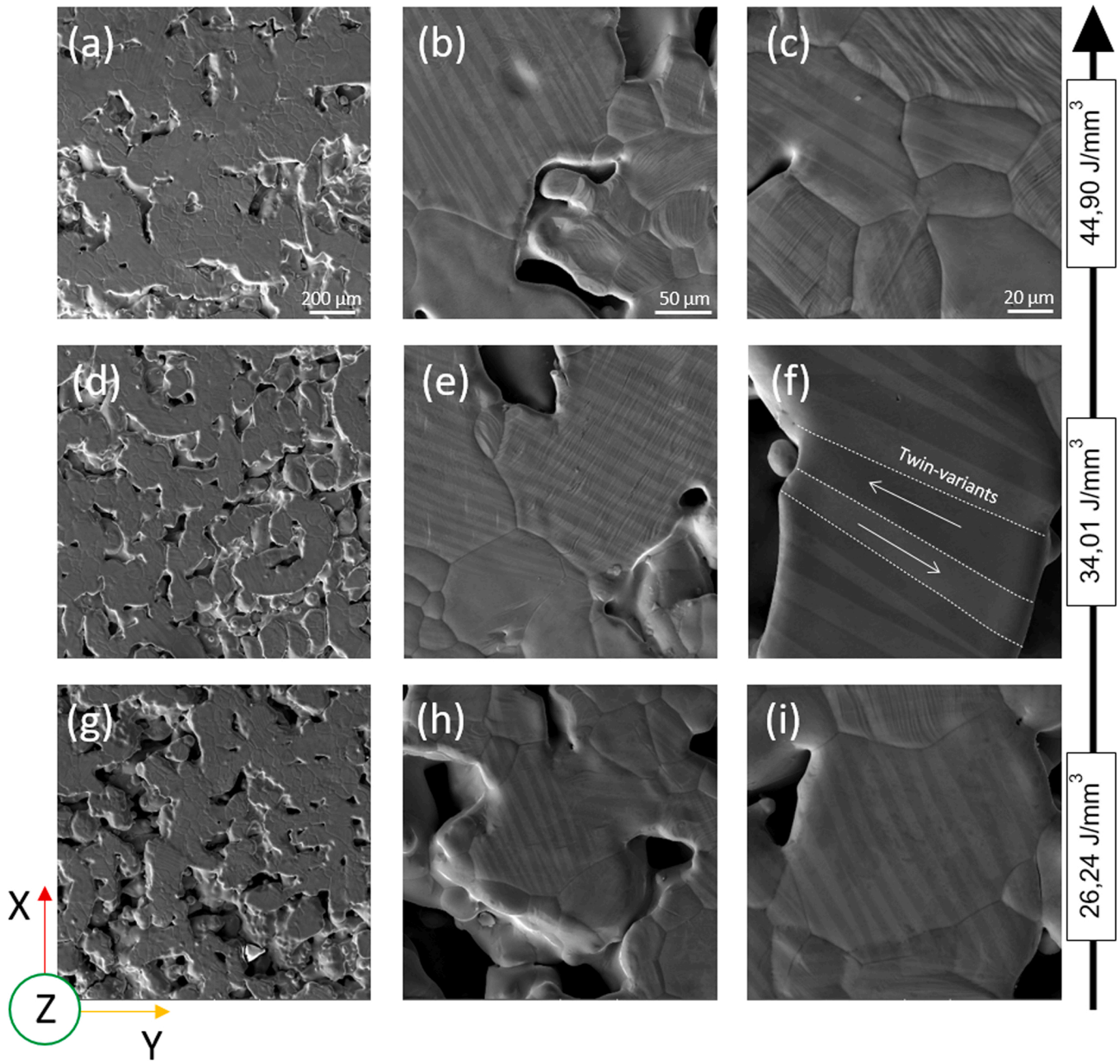


**Fig. 6.** Scanning electron microscopy (SEM) images from top XY plane with min. to max. ED. and different magnifications. From top to bottom: (a), (b), and (c) SMA #7. (d), (e), and (f) SMA #5. (g), (h), and (i) SMA #3.

**Table 5**
ANOVA table for Density (%) and Mn evaporation (%) after heat treatment including P and v terms as continuous predictors.

| | | Mn Evaporation (%) | | | Density (%) | | |
|---|---|---|---|---|---|---|---|
| Source | DF | Sum of Squares | F Ratio | P-value | Sum of Squares | F Ratio | P-value |
| P | 1 | 1.752 | 9.187 | 0.039 | 44.450 | 80.637 | 0.0009 |
| v | 1 | 0.453 | 2.377 | 0.198 | 50.107 | 90.899 | 0.0007 |
| P * P | 1 | 0.131 | 0.687 | 0.454 | 0.705 | 1.279 | 0.321 |
| P * v | 1 | 0.141 | 0.737 | 0.439 | 0.327 | 0.593 | 0.484 |
| Model | 4 | 2.477 | 3.247 | 0.140 | 95.589 | 43.352 | 0.001 |
| Error | 4 | 0.763 | | | 2.205 | | |
| C. Total | 8 | 3.239 | | | 97.794 | | |

The P-value reveals that for Mn evaporation (%) the effect of P is more significant (i.e., P-value = 0.039) when compared to v (i.e., P-value = 0.198). On the other hand, v shows slightly higher significance for density (%) (i.e., P-value = 0.0007). Nevertheless, the effect of P is significant (i.e., P-value = 0.0009). The remaining interaction terms and quadratic effects show lower statistical significance; however, they contribute to the overall effect, hence included in the regression model.

**Table 6**
RSM regression equations for Density (%) and Mn evaporation (%) after heat treatment.

| RMSE | $R^2$ | $R^2$ (Adj.) | Regression |
|---|---|---|---|
| 0.437 | 0.764 | 0.530 | *Mn (%) eva. = 39.032–1.357* P - 0.016* v + 0.01* $P^2$ +0.000375* P*v* |
| 0.742 | 0.977 | 0.955 | *Density (%) = 157.038–2.174* P - 0.0575* v + 0.0237* $P^2$ +0.00057* P*v* |

Fig. 9 shows a clear trend of the porosity formation in the XY slice that indicates a strong influence of the scan strategy. The XZ and ZY slices show preferential XY locations with a significant amount of pattern-like repeated porosity along the build direction. The investigation of the periodic XY preferential locations indicated that the average distance between XY locations of the porosity was 12–13 pixels, corresponding to about ~140 μm, which is also the laser beam width.

The measured Mn % values in the as-built and heat-treated samples indicate that only a small amount of the porosity is caused by the Mn evaporation and most of the porosity is a lack of fusion type. A closer

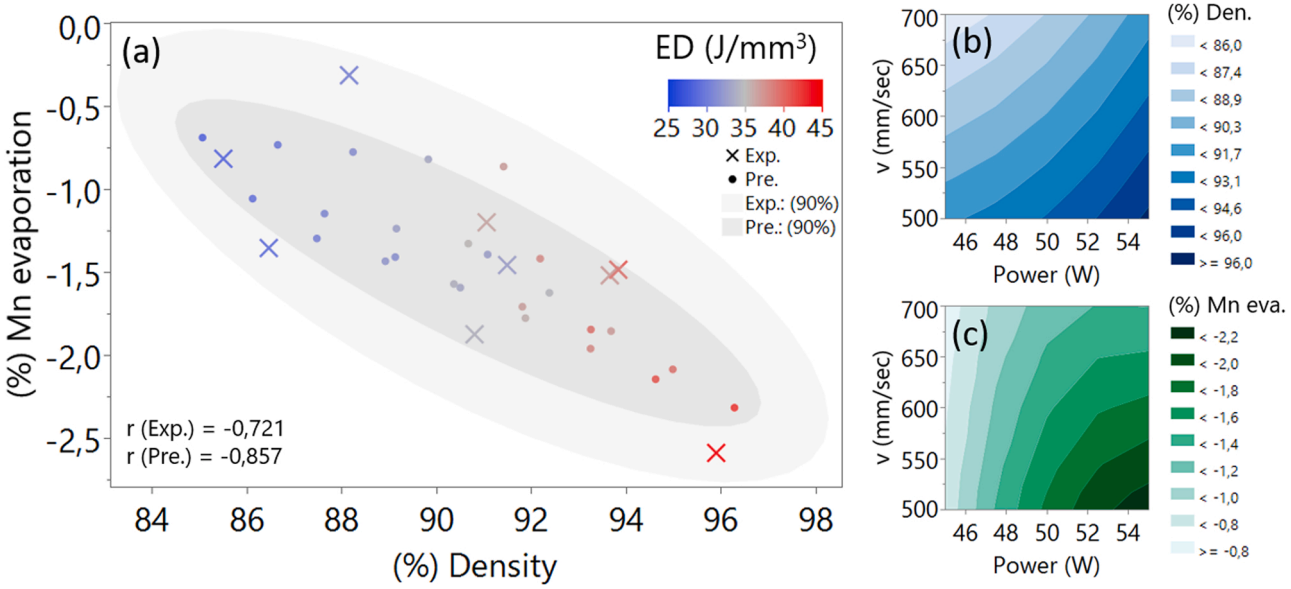


**Fig. 7.** RSM results. (a) Density (%) and Mn (%) evaporation as a function of the volumetric energy density (ED) for experimental (Exp.) and prediction (Pre.) results, and contour plots for (b) Density (%), and (c) Mn (%) evaporation.

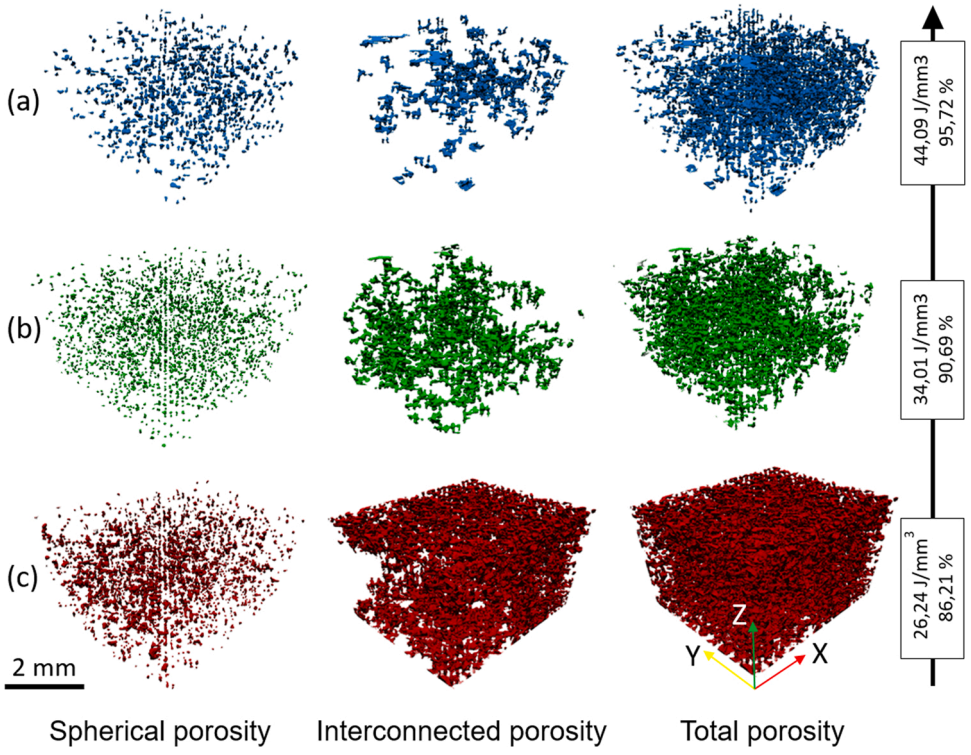


**Fig. 8.** X-ray CT scanning results. 3D view of the density and porosity morphology with varying energy density. (a) Low energy density (LED), (b) mid energy density (MED), and (c) high energy density (HED).

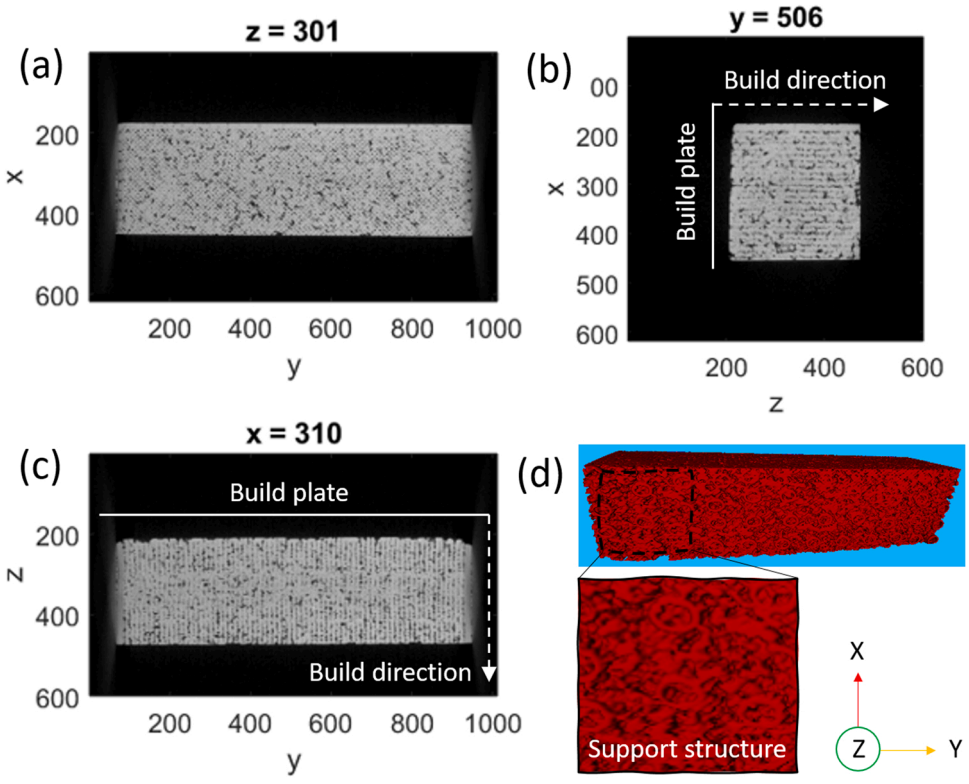


**Fig. 9.** X-ray CT scanning of sample SMA#5 MED with units in pixels. (a) XY slice at Z = 301, (b) XZ slice at Y= 506, (c) ZY slice at X = 310. and (d) 3D view of the sample with reference to the support structures.

look at Fig. 10 shows the distinctive porosity pattern appearing as the ED decreases and overall porosity increases. The yellow areas in the figure reveal the region where lack of fusion is induced as a result of the island scanning strategy. The magnification presented in Fig. 10 (b) and (c) shows a detailed representation of the periodic pattern where the dashed line corresponds to the laser scanning vector.

### 3.4. Magnetic behavior and phase transformation temperatures

Table 7 shows the measured start and end temperatures of martensitic and austenitic transformations and the Curie temperature of the samples. As the structure was ordered and homogenised, and some manganese had evaporated during manufacturing and heat treatment, both austenite and martensite transformation temperatures are slightly higher. In contrast, the Curie temperature is slightly lower than typical for 10 M Ni-Mn-Ga alloy.

In Fig. 11 (a) and (b) the magnetisation results and normalised susceptibility for all samples. The measurements were performed on each sample after the heat treatment step. The magnetic moment (M) is a quantity that describes the magnetic strength of magnetisation of the entire object. During heating up, the transformation from the martensitic structure into austenitic is steep, and the temperature gap between austenitic and martensitic structures is comparatively narrow at 10 degrees considering the structure is polycrystalline, see Fig. 11 (b). The result from Table 7 shows how all the samples have Curie temperature at +/- 2 degrees of each other, and all samples have a similar high magnetisation of 56 $Am^2/kg$, which is within the typical magnetisation range for 10 M Ni-Mn-Ga alloy. Comparative magnetisation values of the samples with those of Ni-Mn-Ga single crystals are possible due to the preferential orientation of grains that has occurred during the laser PBF.

### 3.5. Mechanical testing and MFIS training: preliminary results

The macro mechanical testing confirmed our initial assumption that the Ni-Mn-Ga alloy samples show a brittle fracture due to the high porosity. For example, Fig. 12 shows how the SMA#2 sample was processed at an effective power of 45 W, scanning speed of 600 mm/sec, which resulted in an ED of 30.61 $J/mm^3$ and Archimedes density 88,16 ± 0.56% fractured after a small plastic strain of about 0.02%. The fracture occurred at a total strain of 0.13%, with stress of 19,89 MPa and a yield of above 10 MPa. This strain is typical of multigrain 10 M Ni-Mn-Ga alloy [39–41] and is due to the limited rearrangement of twin structure within the grains, which occurs at a relatively low-stress level. Nevertheless, the estimated yield stress of 10 MPa is still 2–3 times higher than that needed for the magnetically driven shape change present in single crystals [42].

Contact measurements typically perform MFIS characterisation with high accuracy, and in polycrystalline samples, the expected MFIS is often below 0.1% [43,44]. However, the small MFIS can be enhanced by macroporosity, as evidenced by a 0.2% MFIS recorded by Zhang et al. [44]. AM of Ni-Mn-Ga structures with controlled macroporosity can potentially have a small amount of MFIS to be leveraged for sensor and transducer applications.

Concerning macro MFIS characterisation, we could not directly observe and record MFIS using our optical measurements setup. The measured dimensional changes during the rotation were within the measurement error of the optical analysis method (0.2%). In addition to the error during the image analysis, this optical measurement method can also lead to other problems during MFIS measurement. Firstly, attaching the samples using 3 M tape creates constraints that reduce the measured MFIS. Additionally, attaching the samples to the stage using tape can also lead to bending of the sample along the z-direction due to the MFIS, which is not visible in the images or in the analysis. Lastly, when the samples are rotated, it is possible that the focus changes during the movement and increases the measurement error.

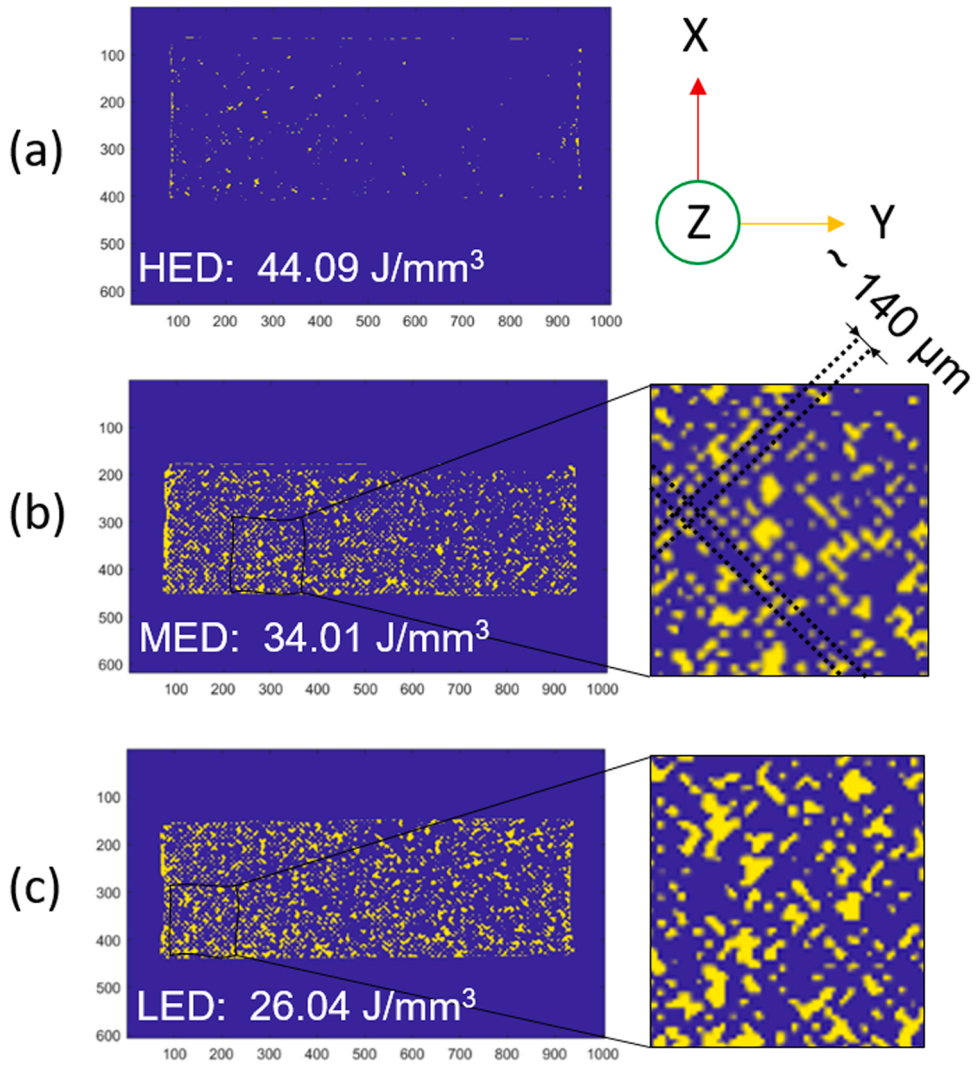


**Fig. 10.** X-ray CT scanning in XY slice with units in pixels. Where the yellow color refers to voids and pores. (a) The high energy density (HED), (b) mid energy density (MED), and (c) low energy density (LED). (For interpretation of the references to colour in this figure legend, the reader is referred to the web version of this article.)

**Table 7**
Phase transformation temperatures of heat-treated samples measured using laboratory built low-field ac susceptibility measurement system.

| Sample (#) | Ms (°C) | Mf (°C) | As (°C) | Af (°C) | Curie (°C) |
|---|---|---|---|---|---|
| SMA 1 | 49.71 | 37.85 | 44.07 | 58.26 | 95.00 |
| SMA 2 | 47.52 | 42.75 | 51.04 | 57.12 | 95.32 |
| SMA 3 | 43.47 | 37.62 | 46.06 | 52.41 | 96.29 |
| SMA 4 | 47.22 | 39.91 | 47.87 | 55.64 | 94.43 |
| SMA 5 | 44.74 | 38.41 | 46.58 | 53.24 | 95.45 |
| SMA 6 | 43.36 | 37.07 | 43.63 | 53.92 | 95.53 |
| SMA 7 | 48.89 | 41.51 | 49.44 | 57.34 | 94.08 |
| SMA 8 | 53.67 | 48.83 | 49.98 | 63.14 | 92.99 |
| SMA 9 | 45.49 | 38.23 | 45.28 | 54.72 | 95.16 |

## 4. Conclusions and future research

Ni-Mn-Ga devices are a promising smart material to produce small devices in which traditional mechanisms and piezoelectric are impractical. Example applications include fast optical and electrical switches, digital pneumatic valves, microfluidic pumps, and micromanipulators. Ni-Mn-Ga alloys have clear potential in applications where a fast-acting actuator device is excited by a magnetic field. However, the cost related to conventional routes for manufacturing and preparation (e.g., casting replication) has hindered commercial applications' development. AM and specially L-PBF show great potential for a cost-effective scale-up method of Ni-Mn-Ga large devices with complex geometries and reproducible as well as significant magnetic-field-induced strain.

This research shows the potential of combining L-PBF and Ni-Mn-Ga powder to tailor microscale and mesoscale features. The ultimate objective is to manufacture geometrically complex devices with visible macroscale MFIS. The control of L-PBF parameters allows tailoring the Ni-Mn-Ga polycrystalline microstructure. Microscale results on chemical composition, crystal structure, and magnetisation measurements validated the initial hypothesis that a delicate trade-off optimisation is present when producing foam like Ni-Mn-Ga structures by L-PBF.

We obtained twinned martensitic structures with a predominant orientation going across the visible grain boundaries. The combination of L-PBF process parameters and heat treatment influences the resulting grain size and number of twins. However, the L-PBF process parameter changes did not significantly influence the crystal structure as the 10 M crystal structure was recovered after the heat treatment in all samples. All the processed samples have a 56 $Am^2/kg$ magnetisation level, the typical magnetisation range for Ni-Mn-Ga 10 M single crystals.

Mesoscale results on density and porosity measurements show that mesoscale tailoring is possible. L-PBF process parameters can be tuned to produce foam-like Ni-Mn-Ga samples. We tailored a distinctive porosity

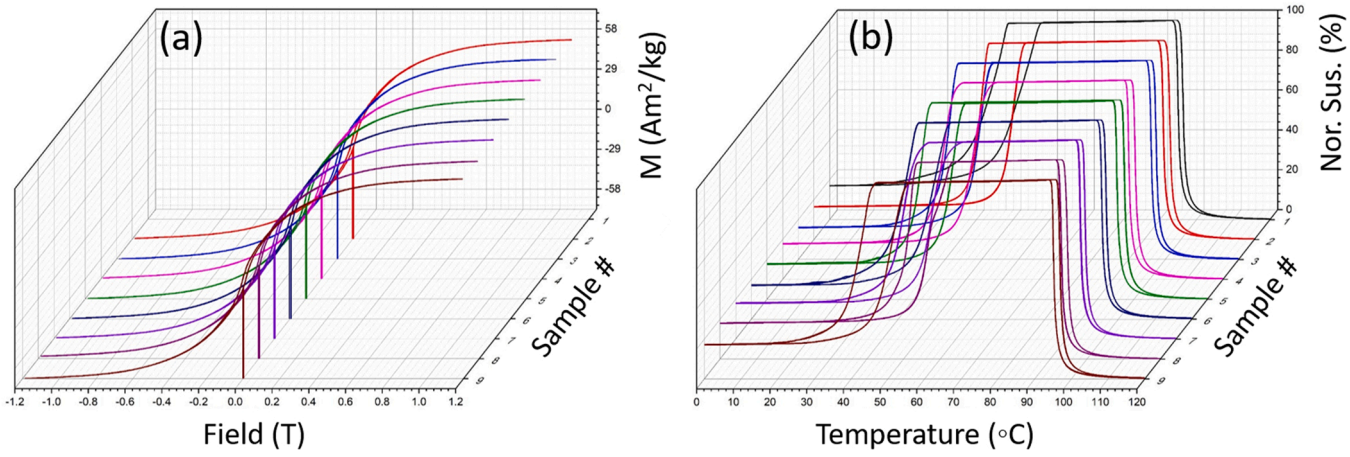


**Fig. 11.** Vibrating sample magnetometer measurements of the homogenised and ordered samples and powder heat-treated at the salt bath at 760 °C for 24 h. [12].

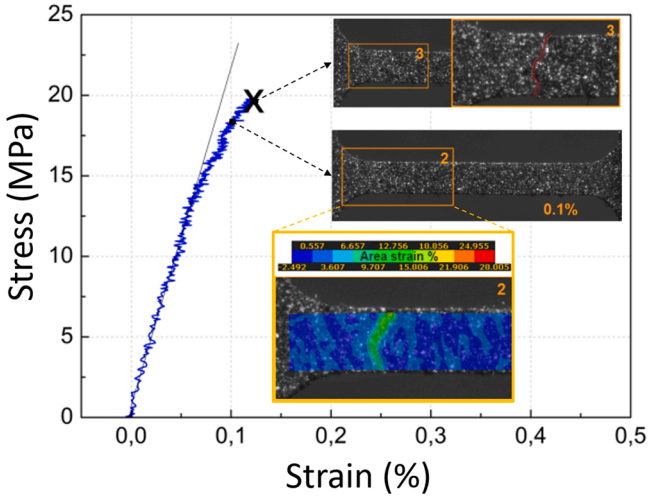


**Fig. 12.** Tensile testing result of miniature tensile rods. SMA#2.

pattern appearing as the ED decreases and overall porosity increases. The implemented island scanning strategy revealed porous regions induced by a lack of fusion. Thus, showing the possibility to create periodic patterns and obtain foam-like Ni-Mn-Ga. However, preliminary macroscale results on mechanical and MFIS characterisation show the expected brittle fracture of samples due to the high porosity. The yield stress is 2–3 times higher than that needed for the magnetically driven shape change in single crystals. Furthermore, MFIS could not be measured reliably, which opens an area for future research.

Overall, these results help us outline research directions that must be explored as several delicate trade-offs need to be overcome. Our experimental approach was limited to a single set of parameters regarding laser-scanning strategy (i.e., 5 × 5 mm island scanning strategy as described in Fig. 2). Two methodologies can be combined to achieve mesoscale tailoring: first, by utilising low ED in selected regions to create areas lacking fusion and second, using higher ED in certain regions to induce the evaporation of alloying elements like Mn. Future research should combine low-ED strategies with experimental island scanning patterns to tailor periodic porous structures at mesoscale and engineer functional foam-like Ni-Mn-Ga complex devices.

As the ED affects the porosity in the samples, an optimal ED range for both porosity and grain size can likely be determined with further experiments. However, this requires to be supported by EBSD characterisation to evaluate quantitatively twinned martensitic structures and predominant orientation going across the visible grain boundaries and its interlink with process parameters. On the other hand, we plan to develop a setup for magneto-mechanical MFIS training using an electromagnet and mechanical compression system. Furthermore, we need to determine the optimal measurement method to characterise MFIS at the macroscale and mechanical testing setup, including compressive test instead of tensile.

In sum, controlling the porosity, together with the orientation and grain size, would make producing the foam-like polycrystalline Ni-Mn-Ga actuators possible as porosity together with grain orientation can be used to reduce grain boundary constraints and thus magnetic force needed for MFIS towards the additive manufacturing of Ni-Mn-Ga complex devices with visible MFIS. Future research is planned to (i) evaluate quantitatively twinned martensitic structures and orientation using EBSD, (ii) to combine distinct energy density and laser-scanning strategies in the same build to tailor periodic porous structures, and (iii) to determine the optimal magneto-mechanical MFIS training and test setup to characterise MFIS at the macroscale towards the additive manufacturing of Ni-Mn-Ga complex devices with visible MFIS.

## CRediT authorship contribution statement

Conceptualization: **Inigo Flores Ituarte, Frans Niels, Simo-Pekka Hannula**. Methodology: **Iñigo Flores Ituarte, Frans Niels, Mika Salmi**. Formal analysis: **Inigo Flores Ituarte, Frans Niels, Venkata Karthik Nadimpalli**. Investigation: **Inigo Flores Ituarte, Frans Niels, Venkata Karthik Nadimpalli, Mika Salmi, Joonas Lehtonen**. Writing – review & editing: **Inigo Flores Ituarte, Frans Niels, Venkata Karthik Nadimpalli, Simo-Pekka Hannula**.

## Declaration of Competing Interest

The authors declare that they have no known competing financial interests or personal relationships that could have appeared to influence the work reported in this paper.

## Acknowledgement

We gratefully acknowledge the support of the Aalto University seed funding for the DEMINFUN-project (974110). Frans Nilsén also acknowledges (in part) support by Operational Program Research, Development and Education financed by European Structural and Investment Funds and the Czech Ministry of Education, Youth and Sports (Project No. SOLID21 - CZ.02.1.01/0.0/0.0/16_019/0000760).

## References


[1] O. Heczko, L. Straka, K. Ullakko, Relation between structure, magnetisation process and magnetic shape memory effect of various martensites occurring in Ni-Mn-Ga alloys, J. Phys. IV Fr. 112 (2003) 959–962, https://doi.org/10.1051/jp4:20031040.

[2] J. Wang, H. Sehitoglu, Twinning stress in shape memory alloys: theory and experiments, Acta Mater. 61 (2013) 6790–6801, https://doi.org/10.1016/j.actamat.2013.07.053.

[3] I. Aaltio, A. Soroka, Y. Ge, O. Söderberg, S.P. Hannula, High-cycle fatigue of 10M Ni-Mn-Ga magnetic shape memory alloy in reversed mechanical loading, Smart Mater. Struct. 19 (2010), https://doi.org/10.1088/0964-1726/19/7/075014.

[4] A. Sozinov, N. Lanska, A. Soroka, W. Zou, 12% magnetic field-induced strain in Ni-Mn-Ga-based non-modulated martensite, Appl. Phys. Lett. 102 (2013), https://doi.org/10.1063/1.4775677.

[5] P. Müllner, Twinning stress of type I and type II deformation twins, Acta Mater. 176 (2019) 211–219, https://doi.org/10.1016/j.actamat.2019.07.004.

[6] Z. Li, Y. Zhang, C. Esling, X. Zhao, L. Zuo, Twin relationships of 5M modulated martensite in Ni-Mn-Ga alloy, Acta Mater. 59 (2011) 3390–3397, https://doi.org/10.1016/j.actamat.2011.02.014.

[7] K. Ullakko, Magnetically controlled shape memory alloys: a new class of actuator materials, J. Mater. Eng. Perform. 5 (1996) 405–409, https://doi.org/10.1007/BF02649344.

[8] S. Barker, E. Rhoads, P. Lindquist, M. Vreugdenhil, P. Müllner, Magnetic shape memory micropump for submicroliter intracranial drug delivery in rats, J. Med. Devices Trans. (2016) 1–6, https://doi.org/10.1115/1.4034576.

[9] K. Ullakko, L. Wendell, A. Smith, P. Müllner, G. Hampikian, A magnetic shape memory micropump: Contact-free, and compatible with PCR and human DNA profiling, Smart Mater. Struct. 21 (2012), https://doi.org/10.1088/0964-1726/21/11/115020.

[10] E. Pagounis, R. Chulist, M.J. Szczerba, M. Laufenberg, High-temperature magnetic shape memory actuation in a Ni-Mn-Ga single crystal, Scr. Mater. 83 (2014) 29–32, https://doi.org/10.1016/j.scriptamat.2014.04.001.

[11] E. Pagounis, A. Laptev, M.J. Szczerba, R. Chulist, M. Laufenberg, Structural behavior and magnetic properties of a Ni-Mn-Ga single crystal across the martensite/austenite two-phase region, Acta Mater. 89 (2015) 32–40, https://doi.org/10.1016/j.actamat.2015.02.001.

[12] F.M.C. Nilsén, Processing and properties of MSM based hybrid materials, Aalto Univ. (2018) https://doi.org/978-952-60-8099-4.

[13] E. Stevens, J. Toman, K. Kimes, V. Chernenko, A. Wojcik, W. Maziarz, M. Chmielus, Microstructural evaluation of magnetocaloric Ni-Co-Mn-Sn produced by directed energy deposition, Microsc. Microanal. 22 (2016) 1774–1775, https://doi.org/10.1017/s1431927616009715.

[14] M.P. Caputo, C.V. Solomon, A facile method for producing porous parts with complex geometries from ferromagnetic Ni-Mn-Ga shape memory alloys, Mater. Lett. 200 (2017) 87–89, https://doi.org/10.1016/j.matlet.2017.04.112.

[15] M.P. Caputo, A.E. Berkowitz, A. Armstrong, P. Müllner, C.V. Solomon, 4D printing of net shape parts made from Ni-Mn-Ga magnetic shape-memory alloys, Addit. Manuf. 21 (2018) 579–588, https://doi.org/10.1016/j.addma.2018.03.028.

[16] S.L. Taylor, R.N. Shah, D.C. Dunand, Ni-Mn-Ga micro-trusses via sintering of 3D-printed inks containing elemental powders, Acta Mater. 143 (2018) 20–29, https://doi.org/10.1016/j.actamat.2017.10.002.

[17] J. Toman, P. Müllner, M. Chmielus, Properties of as-deposited and heat-treated Ni-Mn-Ga magnetic shape memory alloy processed by directed energy deposition, J. Alloy. Compd. 752 (2018) 455–463, https://doi.org/10.1016/j.jallcom.2018.04.059.

[18] V. Laitinen, A. Sozinov, A. Saren, A. Salminen, K. Ullakko, Laser powder bed fusion of Ni-Mn-Ga magnetic shape memory alloy, Addit. Manuf. 30 (2019), 100891, https://doi.org/10.1016/j.addma.2019.100891.

[19] V. Laitinen, A. Salminen, K. Ullakko, First investigation on processing parameters for laser powder bed fusion of Ni-Mn-Ga magnetic shape memory alloy, J. Laser Appl. 31 (2019), 022303, https://doi.org/10.2351/1.5096108.

[20] F. Nilsén, I. Flores Ituarte, M. Salmi, J. Partanen, S.-P. Hannula, effect of process parameters on non-modulated Ni-Mn-Ga alloy manufactured using powder bed fusion, Addit. Manuf. 28 (2019) 464–474, https://doi.org/10.1016/j.addma.2019.05.029.

[21] A. Arabi-Hashemi, X. Maeder, R. Figi, C. Schreiner, S. Griffiths, C. Leinenbach, 3D magnetic patterning in additive manufacturing via site-specific in-situ alloy modification, Appl. Mater. Today 18 (2020), 100512, https://doi.org/10.1016/j.apmt.2019.100512.

[22] I. Flores Ituarte, N. Kretzschmar, A.H. Azman, S. Chekurov, D.B. Pedersen, A. Chaudhuri, Implications of lattice structures on economics and productivity of metal powder bed fusion, Addit. Manuf. 31 (2020), 100947, https://doi.org/10.1016/j.addma.2019.100947.

[23] I. Flores Ituarte, N. Boddeti, V. Hassani, M.L. Dunn, D.W. Rosen, Design and additive manufacture of functionally graded structures based on digital materials, Addit. Manuf. 30 (2019), 100839, https://doi.org/10.1016/j.addma.2019.100839.

[24] J.Y. Lee, J. An, C.K. Chua, Fundamentals and applications of 3D printing for novel materials, Appl. Mater. Today 7 (2017) 120–133, https://doi.org/10.1016/j.apmt.2017.02.004.

[25] D.W. Rosen, Research supporting principles for design for additive manufacturing, Virtual Phys. Prototyp. 9 (2014) 225–232, https://doi.org/10.1080/17452759.2014.951530.

[26] T. DebRoy, T. Mukherjee, J.O. Milewski, J.W. Elmer, B. Ribic, J.J. Blecher, W. Zhang, Scientific, technological and economic issues in metal printing and their solutions, Nat. Mater. (2019), https://doi.org/10.1038/s41563-019-0408-2.

[27] W. Chen, T. Voisin, Y. Zhang, J. Florien, C.M. Spadaccini, D.L. Mcdowell, T. Zhu, Y. M. Wang, Microscale residual stresses in additively manufactured stainless steel, Nat. Commun. (2019) 1–12, https://doi.org/10.1038/s41467-019-12265-8.

[28] R. Shi, S.A. Khairallah, T.T. Roehling, T.W. Heo, J.T. McKeown, M.J. Matthews, Microstructural control in metal laser powder bed fusion additive manufacturing using laser beam shaping strategy, Acta Mater. 184 (2020) 284–305, https://doi.org/10.1016/j.actamat.2019.11.053.

[29] T.T. Roehling, R. Shi, S.A. Khairallah, J.D. Roehling, G.M. Guss, J.T. McKeown, M. J. Matthews, Controlling grain nucleation and morphology by laser beam shaping in metal additive manufacturing, Mater. Des. 195 (2020), 109071, https://doi.org/10.1016/j.matdes.2020.109071.

[30] L.N. Carter, C. Martin, P.J. Withers, M.M. Attallah, The influence of the laser scan strategy on grain structure and cracking behaviour in SLM powder-bed fabricated nickel superalloy, J. Alloy. Compd. 615 (2014) 338–347, https://doi.org/10.1016/j.jallcom.2014.06.172.

[31] P. Köhnen, M. Létang, M. Voshage, J.H. Schleifenbaum, C. Haase, Understanding the process-microstructure correlations for tailoring the mechanical properties of L-PBF produced austenitic advanced high strength steel, Addit. Manuf. 30 (2019), 100914, https://doi.org/10.1016/j.addma.2019.100914.

[32] T. Mukherjee, T. DebRoy, A digital twin for rapid qualification of 3D printed metallic components, Appl. Mater. Today 14 (2019) 59–65, https://doi.org/10.1016/j.apmt.2018.11.003.

[33] M. Chmielus, X.X. Zhang, C. Witherspoon, D.C. Dunand, P. Müllner, Giant magnetic-field-induced strains in polycrystalline Ni–Mn–Ga foams, Nat. Mater. 8 (2009) 863–866, https://doi.org/10.1038/nmat2527.

[34] S. Joshi, K. Rawat, K.C. Rajamohan V., A.T. Mathew, K. Koziol, V. Kumar Thakur, B. A.S.S, 4D printing of materials for the future: opportunities and challenges, Appl. Mater. Today 18 (2020), 100490, https://doi.org/10.1016/j.apmt.2019.100490.

[35] V. Laitinen, A. Sozinov, A. Saren, M. Chmielus, K. Ullakko, Characterisation of as-built and heat-treated Ni-Mn-Ga magnetic shape memory alloy manufactured via laser powder bed fusion, Addit. Manuf. 39 (2021), 101854, https://doi.org/10.1016/j.addma.2021.101854.

[36] S. Roth, U. Gaitzsch, M. Pötschke, L. Schultz, Magneto-mechanical behaviour of textured polycrystals of NiMnGa ferromagnetic shape memory alloys, Adv. Mater. Res. 52 (2008) 29–34, https://doi.org/10.4028/www.scientific.net/amr.52.29.

[37] V.A. Chernenko, Compositional instability of β-phase in Ni-Mn-Ga alloys, Scr. Mater. 40 (1999) 523–527, https://doi.org/10.1016/S1359-6462(98)00494-1.

[38] A. Armstrong, F. Nilsén, M. Rameš, R.H. Colman, P. Veřtát, T. Kmječ, L. Straka, P. Müllner, O. Heczko, Systematic trends of transformation temperatures and crystal structure of Ni–Mn–Ga–Fe–Cu alloys, Shape Mem. Superelasticity 6 (2020) 97–106, https://doi.org/10.1007/s40830-020-00273-3.

[39] U. Gaitzsch, M. Pötschke, S. Roth, B. Rellinghaus, L. Schultz, A 1% magnetostrain in polycrystalline 5M Ni–Mn–Ga, Acta Mater. 57 (2009) 365–370, https://doi.org/10.1016/j.actamat.2008.09.017.

[40] M. Chmielus, C. Witherspoon, R.C. Wimpory, A. Paulke, A. Hilger, X. Zhang, D. C. Dunand, P. Müllner, Magnetic-field-induced recovery strain in polycrystalline Ni-Mn-Ga foam, J. Appl. Phys. 108 (2010), https://doi.org/10.1063/1.3524503.

[41] N. Scheerbaum, O. Heczko, J. Liu, D. Hinz, L. Schultz, O. Gutfleisch, Magnetic field-induced twin boundary motion in polycrystalline Ni-Mn-Ga fibres, New J. Phys. 10 (2008), https://doi.org/10.1088/1367-2630/10/7/073002.

[42] F. Nilsén, I. Aaltio, S.P. Hannula, Comparison of magnetic field controlled damping properties of single crystal Ni-Mn-Ga and Ni-Mn-Ga polymer hybrid composite structures, Compos. Sci. Technol. 160 (2018) 138–144, https://doi.org/10.1016/j.compscitech.2018.03.026.

[43] M.P. Caputo, A.E. Berkowitz, A. Armstrong, P. Müllner, C.V. Solomon, 4D printing of net shape parts made from Ni-Mn-Ga magnetic shape-memory alloys, Addit. Manuf. 21 (2018) 579–588, https://doi.org/10.1016/j.addma.2018.03.028.

[44] X.X. Zhang, C. Witherspoon, P. Müllner, D.C. Dunand, Effect of pore architecture on magnetic-field-induced strain in polycrystalline Ni-Mn-Ga, Acta Mater. 59 (2011) 2229–2239, https://doi.org/10.1016/j.actamat.2010.12.026.